Thermally Reflowed Die-Attached Linear Variable Optical Filter for Mid-Infrared Volatile Organic Compounds Detection

Simon Chun Kiat Goh, Li Lynn Shiau, Chengkuo Lee, and Chuan Seng Tan

***Abstract*— Accidental or deliberate discharge of industrial chemicals into the environment has to be identified rapidly. Given its ease of fabrication and possibly low-cost operation, linear variable optical filter (LVOF), have been explored as on-chip mid-infrared optical engines. In this work, highly precise and replicable LVOF taper was demonstrated by sandwiching photoresist pillars between two Si-SiO_2 dielectric Bragg reflector deposited Si wafers to form a LVOF. By varying the pillar height, different wedge angles were achieved. It was shown that as wedge angle varied from 0.0786° to 0.0205°, full width half maximum measured at 3.70 μm improved from 320 nm to 220 nm while transmission intensity increased by 35%. LVOF operating range was revealed to be inversely proportional to the wedge angle. Furthermore, the temperature insensitive filter was demonstrated to qualify the presence of vapor ethanol. Finally, LVOF design principles with respect to integrated linear array detectors were discussed. [2019-0101]**

***Index Terms*— Linear variable optical filter, spectroscopy, Si-SiO_2, mid infrared, Fabry-Perot, interferometer.**

I. Introduction

MANY laws have been passed to control industrial emission in most countries around the world. Despite that, chemicals are continuously released into the environment. It is well known that long term exposure to some of these chemicals could potentially degrade our health and that of nature [1], [2]. In order to control the situation, it is imperative to possess the proper monitoring tools. Hitherto, these tools include gas chromatography, mass spectrometry, terahertz spectrometry, infrared spectrometry, etc [3]. Among them, infrared (IR) spectrometry is a field-proven technology that is relatively low cost and is easy to deploy rapidly in the field [4]. Today, miniaturized optical spectrometers are fast revolutionizing industrial processes across many industries such as gas sensing and cell monitoring [5]. At the same time, it empowers consumers by allowing individuals to conduct food analysis, health monitoring, taking local air quality measurements, etc [6], [7]. Infrared spectrometry works by comparing the sample-passed signal with that of the background scan which was carried out in the absence of the analyte(s). In the case of absorption spectroscopy, transmission peaks position are used to identify chemical species. Typically, collected signals are compared with a database such as HiTRAN [8].

A complete IR absorption-based spectrometer anatomy comprises an IR source, optical engine (filter or non-filter type), detector as well as other optical components such as mirrors and lens. Amongst all, the heart of a spectrometer is the optical engine. Various kinds of engines such as grating, prism, photonic crystal, Fabry-Perot interferometer (FPI), and Michelson interferometer based FTIR have been explored as possible on-chip spectrometers [9]–[14]. As the working space in a miniaturized spectrometer is significantly smaller than that of a benchtop spectrometer, certain types of optical engines are preferred. Typically, micro-opto-electro-mechanical systems (MOEMS) FPI and FTIR are often employed in miniaturized spectrometers [15]. Although a FTIR offers high resolution and broad scanning range, the need for precise tracking of the movable mirror and its susceptibility to mechanical vibrations could jeopardize its use as a low-cost and portable miniaturized spectrometer [16]. On the other hand, a tunable MOEMS FPI works by scanning the entire designed operating range by varying the resonant cavity distance between two mirrors. Drawbacks of FPI include, prone to mechanical vibration and signal distortions and long scan time [17].

To overcome the inherent problem with moving parts, the principle of FPI can be extended by tilting one pair of the mirror by an angle to form a fixed Linear Variable Optical Filter (LVOF) [18]. In this case, the cavity distance between two mirrors varies linearly from one end of the filter to another. This way, transmission passbands vary linearly with the change in cavity distance. Typically, the wedge (taper) angle of a LVOF is in the range of tenths of millidegrees. Generally, small wedge angle is preferred over large wedge angle as the latter could results in significant "light runaway" effect [19]. The consequences of a poorly fabricated LVOF taper are: 1) broad full width half maximum (FWHM), and 2) low or no optical transmission. Until now, a number of methods have been demonstrated to create LVOF taper [20]–[27]. Unfortunately, many of the mentioned techniques are only able to produce a small batch of LVOF per run. Moreover, for many of the demonstrated techniques

Manuscript received May 2, 2019; revised August 11, 2019; accepted August 14, 2019. Subject Editor L. Lin. This work was supported by the National Research Foundation Singapore under Grant NRF-CRP001-019. *(Corresponding authors: Simon Chun Kiat Goh; Chuan Seng Tan.)*

S. C. K. Goh, L. L. Shiau, and C. S. Tan are with the School of EEE, Nanyang Technological University, Singapore 639798 (e-mail: gohc0075@e.ntu.edu.sg; tancs@ntu.edu.sg).

C. Lee is with the Department of Electrical and Computer Engineering, National University of Singapore, Singapore 117576.

Color versions of one or more of the figures in this article are available online at http://ieeexplore.ieee.org.

Digital Object Identifier 10.1109/JMEMS.2019.2936006

as discussed above, error incurred during any phase of the fabrication process would render the sample useless without the possibility of rework.

In this work, we demonstrated a highly precise, high yield and good batch-to-batch LVOF fabrication technique using patterned photoresist (PR) as stumps to create the LVOF milli-degree tapered air gap between two dielectric Bragg reflector coated (DBR) silicon (Si) wafers. In this paper, LVOFs with different wedge angles were produced and characterized. Their performances were compared with simulation. Lastly, to show the working capability of the LVOF, volatile organic compounds (VOCs) quantification was demonstrated using ethanol (EtOH).

II. Methodology

A. DBR Fabrication

SiO_2 was deposited using plasma enhanced chemical vapor deposition (PECVD). Deposition of 770 nm of SiO_2 was conducted at 300 °C onto a 6" Silicon (Si) (100) wafer with TEOS as Si precursor. Amorphous Si (a-Si) thin film was sputtered using 99.99% pure undoped Si target. The system was evacuated to a base pressure of 10^{-5} mbar and 50 sccm of Ar was charged into the sputtering chamber. The plasma was maintained with a forward power of 300 W. The deposition on Si substrate was repeated once more to achieve the following configuration: Substrate – SiO_2 – a-Si – SiO_2 – a-Si.

B. LVOF Fabrication

Si/SiO_2 deposited Si wafers were mechanically diced to obtain dies of dimension 10 mm × 10 mm. Thereafter, the wafers were cleaned in acetone and then in isopropanol under agitation to remove particles from the surface. Soft bake process was done in an enclosed hot plate. Three drops of AZ 5214E photoresists were dispensed and the wafer was spin coated at 3000 rpm for 30 s. It was soft baked at 105 °C for 30 s. Another three drops of AZ 5214E were dispensed and spin coated at 3000 rpm for 30 s. It was then soft baked at 105 °C for 120 s. Circular patterns were lithographically transferred to the resist using a mask aligner. Subsequently, the wafer was manually developed using AZ developer diluted 1:2 with deionized water for about 1.25 min. In the case of AZ 9260, the resist was spin coated at 6000 rpm for 30 s and soft baked 105 °C for 200 s. Thereafter, it was developed in AZ developer without dilution. AZ 4620 was coated onto the substrate as follows. AZ 4620 was spin coated at 2000 rpm for 60 s. The coated wafers were soft baked at 130 °C in the described sequence: 60 s non-contact above the hot plate and then followed by 180 s with hot plate contact. Finally, the wafers were cured without contact with the hot plate for 60s. The PR was developed in AZ developer without further dilution.

Later, a piece of 8 mm × 5 mm un-patterned, Si/SiO_2 DBR layers deposited wafer was manually flipped onto the patterned bottom die. One end of the flipped wafer was positioned on top of the PR stumps. The unit was then heated at 150 °C for 1 h on a covered hot plate to allow the PR to reflow. The entire fabrication process is graphically depicted in Fig 1.

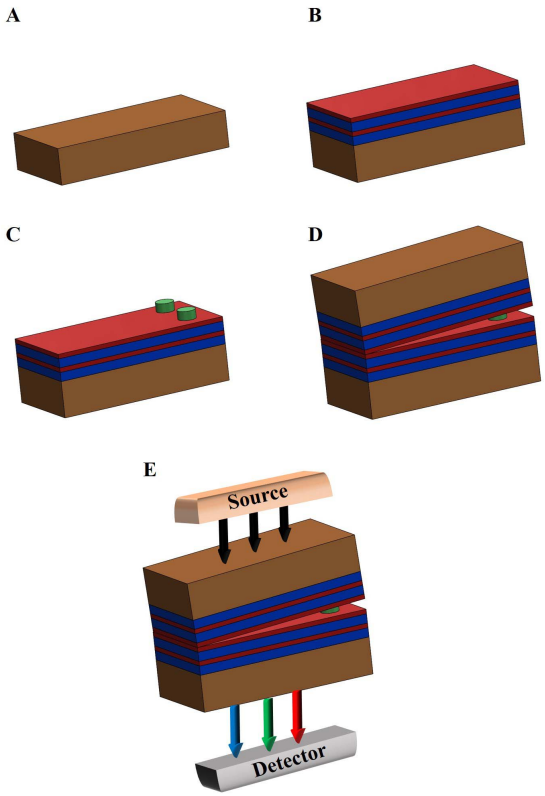

Fig. 1. Fabrication steps to construct a die attached LVOF. A) Si wafers were mechanically diced to 10 mm × 10 mm and were then ultrasonically cleaned in acetone and IPA. B) Thin films of Si and SIO2 were deposited using sputter and PECVD, respectively. C) PR stumps were patterned on the wafers using photolithography. D) A piece of thin film deposited Si without PR stumps (B) was flipped onto (C). The sample was then thermally reflowed. E) Characterization of LVOF was performed using a benchtop FTIR.

For characterization of the patterned resist only, the wafer was reflowed in the absence of a top die.

C. Ethanol (EtOH) Vapor Preparation

Absolute ethanol (Puriss grade) obtained from Sigma-Aldrich was used directly without further purification. An amount of EtOH was dispensed onto a cleaned borosilicate glass petri dish using a syringe. The enclosed petri dish "gas cell" was clamped tightly to prevent leakage. Then, it was heated on a hotplate at 75 °C for about 1-2 min to allow the EtOH to vaporize.

III. Characterization

Electron microscopy was performed using a field emission-scanning electron microscopy (FESEM, JEOL JSM-7600F.) The acceleration voltage was set to 5 kV to prevent surface charging from occurring. Atomic force microscopy (AFM) was performed on a Bruker Dimension. The sampling area was set to 100 μm x 100 μm with a scan rate of 1 Hz. A total of 512 lines were scanned. Surface profiling was conducted using a Detak XT profiler. A scan length of 1000 μm at a scan rate of 50 μm/s was used. Grazing angle XRD was performed on a Bruker D8 using detector scan mode. 2θ was measured

between 20° and 80°. Refractive index and extinction coefficient were measured at 55°, 65°, and 75°, respectively, on a JA Woollam angle variable ellipsometer. Raman spectroscopy was performed using a 532 nm excitation laser source on a UHTS300 Raman spectrometer (Witec) with 600 g/mm grating. FTIR was conducted on an Agilent Cary 620 from 2 – 8 μm with a resolution of 16 cm^{-1} in transmission mode and an aperture size of 100 μm x 100 μm was set. A 100X objective lens enabled focusing on the back of the flipped top wafer. Prior to testing, reference background was conducted in the air in the absence of any sample. For EtOH vapor characterization, a new background was taken in the presence of the gas cell. For EtOH measurement, the EtOH-filled gas cell was positioned in between the IR source and the fabricated LVOF.

IV. Results and Discussion

The DBR was designed using Lumerical FDTD with center passband at 3.7 μm. DBR comprises an alternating layer of high and low refractive materials. Sputtered Si and SiO_2 were specifically chosen as the high refractive index (H, n_H) and low refractive index material (L, n_L) and the DBRs were separated by an air gap. Both quarter and half wave stacks were designed with resonance mode (m = 1). At 3.7 μm, the Bragg contrast, which is defined as the ratio of n_H/n_L of Si/SiO_2 is approximately 2.0. The use of Si and SiO_2 enables one to achieve high Bragg contrast with fewer deposition layers. It could minimize fabrication issues associated with a large number of DBR layers such as coating stress [28]. This could lead to better fabrication consistency between sample batches. As reported previously, increasing the number of [HL] pairs decreases FWHM of passband [29]. However, it also leads to a decrease in transmission %. In this case, the fabrication of [HLH] -wedge – [HLH] is sufficient for reasonable FWHM and transmission %.

As the wedge angle between the top and bottom mirrors is typically in the range of milli-degrees, LVOF can be approximated either as FPI or Fizeau interferometer. The difference between them is that the latter model would account for transmission intensity loss due to walkaway effect which is significant at higher mode (m>3). Since the quarter and half wave stacks were designed at m = 1, the LVOF can be appropriately approximated as an array of Fabry-Perot resonators [30, 31]. Using this approximation, the top DBR mirror was placed parallel to the bottom DBR mirror during the simulation. Refractive index of sputtered silicon, $n_{Si} = 2.8$, ascertained by ellipsometry, was employed in all FDTD simulations. Sputtered Si has a different refractive index from crystalline Si due to a variation in atomic density and polarizability as described by Claudius-Mossotti relation [32]. FDTD simulated data is shown in Fig 2. It can be seen that the FWHM is 170 nm at 3.70 μm. To simulate the passbands of a LVOF, the top DBR was varied at an interval of 0.25 μm from 1.5 to 2.5 μm with respect to the bottom DBR. The designed LVOF was shown to possess a working range from 3.4 to 4.6 μm. One distinct trait of a cavity varying FPI is an observable increase in FWHM at a longer wavelength.

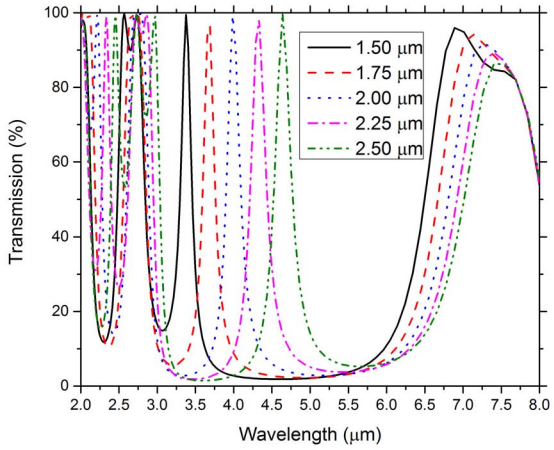

Fig. 2. Simulated passbands of an optical filter with parallel DBRs. Passbands red shifted when inter-DBR cavity distance increases. Meanwhile, it can be noted that FWHM increases with longer passbands from 3.4 to 4.4 μm.

Grazing angle XRD was performed at 1° using detector scan mode to acquire as much information from the sputtered Si layer as possible. To obtain accurate information of the thin film layer without interference, Si and SiO_2 layers were deposited on Si substrate once. As shown in Fig 3A, a small peak was found around 56.0°. According to JCPDS card 00-027-1402, the diffraction peak corresponds to Si (311). However, the absence of distinct peaks at 28.5°, 47.4° and 76.8° suggest that the sputtered Si thin film is amorphous in nature [33], [34].

Raman spectroscopy was performed on sputtered Si on SiO_2 samples. Raman shift between 100 and 700 cm^{-1} was plotted in Fig 3B. Peaks present at 150, 460 cm^{-1} correspond to transverse acoustic and transverse optical, respectively [35]. The absence of the peak at 520 cm^{-1} confirms the amorphous nature of the deposited Si film.

Cross-sectional SEM, as shown in Fig 3C, was used to determine the thickness of the deposited thin films. It can be observed that the thickness of the a-Si layer is approximately 340 nm while that of the SiO_2 layer is roughly 790 nm. A cross-sectional analysis was performed on three random sites to check the thin film for consistency. It was shown that the thin films thicknesses were consistent across the entire wafer. This was done to ensure that LVOFs fabricated from the wafer would have similar optical characteristics.

AFM was carried out to determine the surface roughness of the fabricated samples as shown in Fig 3D. The measured root mean square (R_q) surface roughness of the stacked DBR topmost layer was 4.12 nm. It is well known that rougher surface contributes to light scattering which results in propagation loss [36]. DBR surface roughness is especially critical as light scattering would affect the FWHM of the transmission passband. In any case, low surface roughness is always preferred when fabricating optical filters. In the same light, the calculated optical flatness of this filter is taken to be $\lambda/800$.

To cross check with the FESEM obtained thickness measurement as well as to obtain optical constants, an ellipsometric analysis was carried out with a light source and

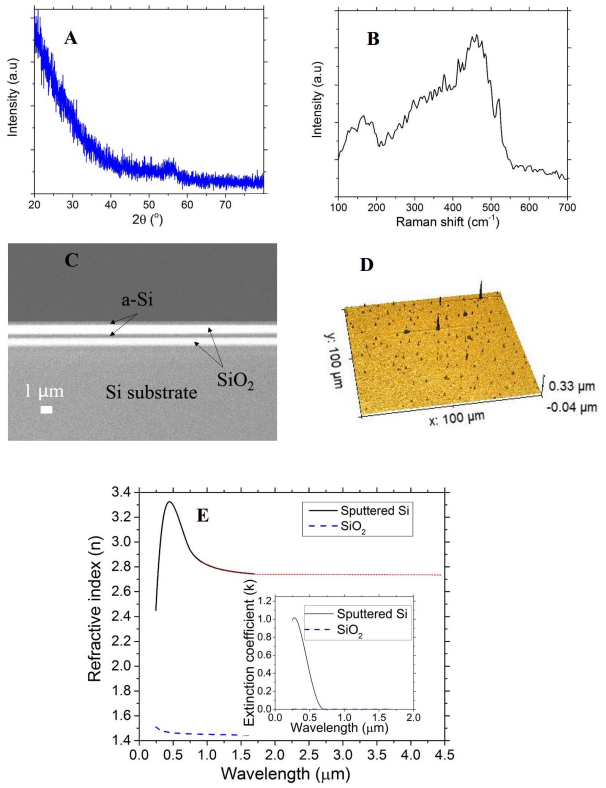

Fig. 3. A) Grazing angle acquired XRD pattern of sputtered amorphous Si, B) Raman shift of sputtered Si on SiO_2, C) cross-sectional FESEM image of the deposited thin film. The fabricated DBR consists of [Si-SiO_2-Si-SiO_2] layers. D) Representative AFM image showing the surface topography of the topmost Si layer and E) Ellipsometry analysis of sputtered Si and PECVD deposited SiO_2.

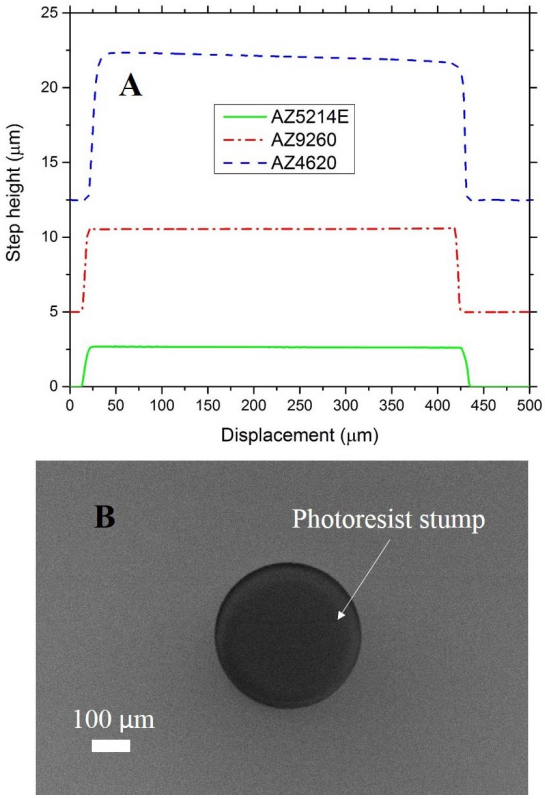

Fig. 4. A) Patterned photoresists and their associated step heights measured using surface profilometer and B) SEM image of a PR stump.

detector up to 1.70 μm. Si and SiO_2 layers were separately deposited on ultrasonically cleaned Si wafers using similar deposition recipes that would be used during actual device fabrication. Ellipsometric results are shown in Fig 3E. Such a method allows simpler ellipsometric analysis without the need to fit Si-SiO_2 DBR construction which could possibly complicate the entire analysis process. The fitted refractive index (n) and extinction coefficient (k) curves for sputtered a-Si and SiO_2 are shown in Fig 3E. Although one is unable to measure directly the optical constants between 3–5 μm due to the lack of appropriate extended source and detector, n and k values could be extrapolated like previous work [37]. The extrapolated n and k values were taken to be 2.8 and 0.0 between 3–5 μm, respectively. The values acquired were consistent with previously reported data [38]. Meanwhile, the thicknesses of Si and SiO_2 were fitted to be 350 and 770 nm, respectively. The ellipsometric data corroborates the thickness measured by cross-section SEM.

Three different types of positive resists were used in this report to achieve dissimilar wedge angles. Surface profiler was used to measure the height of the patterned resists. As shown in Fig 4A, AZ 5214E, AZ 9620 and AZ 4260 pillar height were measured to be approximately 2.5, 5.4 and 9.6 μm, respectively. In turn, these height profiles translate to produce wedge angles of 0.0205°, 0.0442° and 0.0786°, respectively. Thereafter, the samples were annealed and characterized optically to understand the effects of varying wedge angle on FWHM and transmission intensity. Top view SEM imaging, as shown in Fig 4B, was performed to illustrate the patterned resist on Si. The photoresist stumps provided a graduated height difference when two DBR coated Si substrates were thermally bonded to create a LVOF. The main advantage of this method is that the PR height, and the associated wedge angle, could be precisely controlled by manipulating the spin speed or by using a different PR. Therefore, the described method enables one to make micro adjustments to tailor LVOF for specific applications.

To demonstrate that the proposed method is appropriate even for mass production, 4" wafers with Si-SiO_2 DBR were coated with AZ 5214E PR. A photomask with numerous pairs of stump patterns was used for pattern transfer. The height of patterned PR stumps on the wafers was characterized using a step profiler after thermal annealing. A total of 10 points at different locations were measured on each wafer. As shown in Fig 5, the Si-SiO_2 DBR surface was profiled with the mean taper angles and standard variation plotted with respect to different spin speed. A small variation in taper angle suggests excellent control by spin coating.

One of the advantages of the proposed method is that spin coating resist using a highly planar chuck will ensure that the coated resist thickness is uniform on the substrate as explained earlier. In addition, precise replication of patterns is possible with proper control of the thermal reflow procedure. The profile of reflowed PR depends on interfacial tension and its behaviour can be predicted by Young's equation (1) [39]. This leads to uniform PR profile between samples as reported

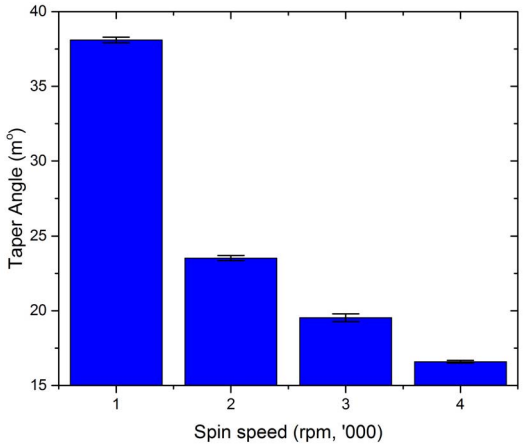

Fig. 5. Taper angles and standard deviations of thermally annealed AZ 5214E PR spin coated at different spin speed.

previously [40].

$$\gamma sv = \gamma sl + \gamma lv cos\theta \tag{1}$$

where $\Upsilon_{sv}, \Upsilon_{sl}, \ and \ \Upsilon_{lv}$ refer to interfacial tensions between substrate and air, substrate and PR and PR and air, respectively. θ is the contact angle between PR and substrate.

Still, variations in local and global angle can be further mitigated by using an automatic developer dispensing tool. At present, we obtained good dies with a yield of more than 90 % with less than 10% of the dies debonded due to rough handling during transport.

For this lab-scale demonstration, each die was manually stacked using a sharp tweezer while viewing under 5X and 10X magnification. This process can be scaled up by using automatic die-attach (flip-chip) die bonders. Current state-of-the-art Die / Flip Chip bonder such as ASM NOVA Plus has a placement accuracy of +/− 2.5 μm [41].

Fabricated samples were then subjected to FTIR measurement. Prior to measurement, background reference was performed in air. In view of reflection at Si-air interfaces due to high Bragg contrast between Si and air, it is expected that the total transmission intensity is lower than simulation as shown in Fig 2. Moreover, Si-SiO_2 DBR was patterned on single side polished Si wafers. The rough Si backside further attenuates transmission signal which contributed to lower transmission intensity. Thus, it would be ideal that double side polished wafers with anti-reflective coated backside to be used in subsequent work. Samples were placed flat on the microscope stage and the normal incidence beam was focused on the backside of the flipped die. Measurements were taken as the microscope stage was translated manually from smaller to larger cavity gap with a step size of 100 μm. The results of AZ 5214E, AZ 9260 and AZ 4620 supported LVOFs were plotted in Fig 6A, B and C, respectively.

As shown in Fig 6, non-overlapping transmission bands for AZ 5214E, AZ 9260 and AZ 4620 samples were shown to be between 3.50 – 4.35 μm, 3.60 – 4.25 μm and 3.75 – 4.35 μm, respectively. In this context, the LVOF operating range is defined by the distance between the mid-points of the straddling stop bands. Operating range of AZ 5214E

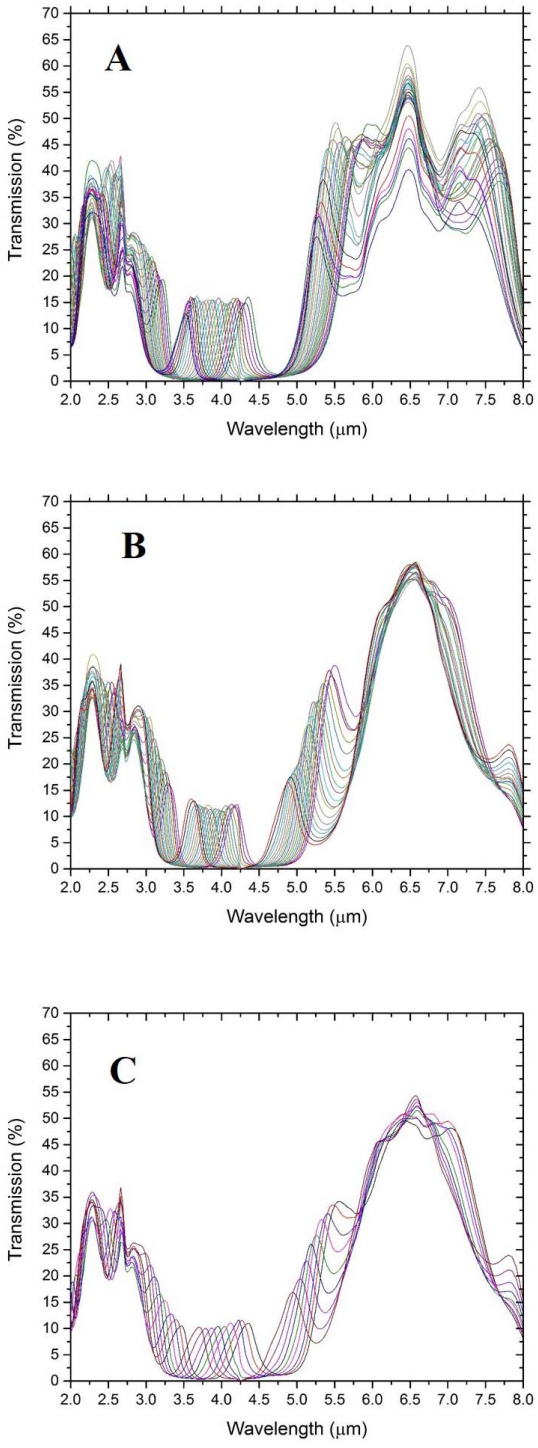

Fig. 6. Transmission profiles of LVOF fabricated with A) AZ 5214E, B) AZ 9620 and C) AZ 4620 PRs which corresponds to wedge angles of 0.0205°, 0.0442° and 0.0786°, respectively. It can be observed that the smaller wedge angle provides a larger operating window as well as higher transmission intensity than LVOF made with a larger wedge angle.

is shown to be between 3.25 and 5.00 μm. However, when the wedge angle increases, the operating range decreases to 3.50 – 4.75 μm in the case of AZ 4620 PR made stumps. The phenomenon can be explained by expanding the concept proposed by Garmire [42]. Generally, all three PR-made LVOF possess almost similar stop bands profiles. On closer

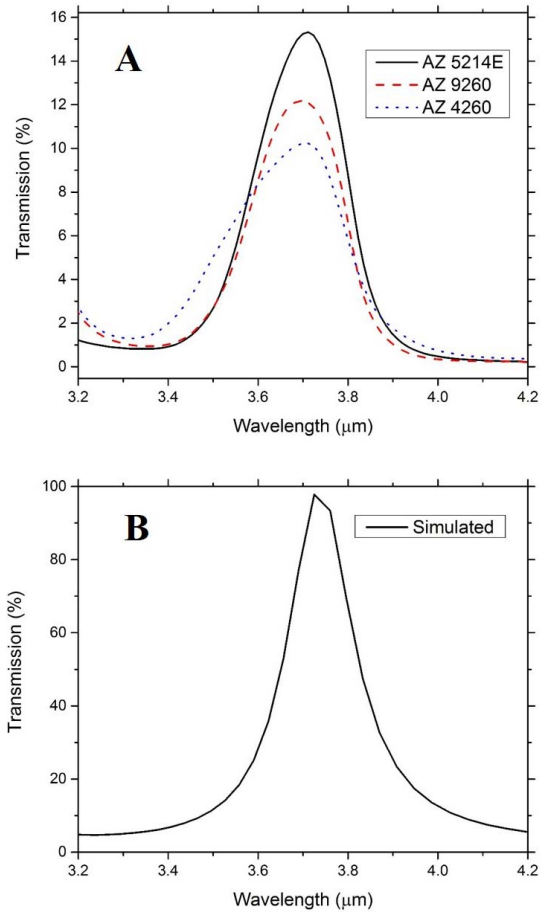

Fig. 7. A) Difference in transmission intensity and FWHM when different PRs were used as stacks. B) FDTD simulated peak for a FPI centered at 3.7 μm.

inspection, overall transmission intensity of peaks of LVOF made with different PRs can be arranged in the following order (Highest to lowest): AZ 5214E, AZ 9260 and AZ 4620.

Extending the work reported by Garmire and with reference to Fig 8, the relationship between LVOF operating range of LVOF and wedge angle α is as shown in Eq (2).

$$LVOF\ operating\ range = \frac{\frac{\lambda^2}{2x\tan\alpha}}{1-\left(\frac{\lambda}{4x\tan\alpha}\right)^2} \tag{2}$$

where λ *is the collimated incidental wavelength,* x is the length of the LVOF and $x\ tan\ \alpha$ *be the* optical path length. *Since* $x \gg \lambda$, *equation* (2) *can be approximated to be*

$$LVOF\ operating\ range \propto \frac{1}{x\tan\alpha} \tag{3}$$

From equation (3), it can be observed that the working range is inversely proportional to α. In which, larger wedge angle will decrease the filter working range. Thus, it confirms the trend of experimentally gathered data as shown in Fig 6.

The quality of the assembled optical filters was examined at 3.70 μm. As shown in Fig 7A, the measured FWHM at 3.70 μm were 220, 250 and 320 nm for AZ 5214E, AZ 9260 and AZ 4620, respectively. As a comparison, as shown in Fig 7B, FWHM of FDTD simulated passband

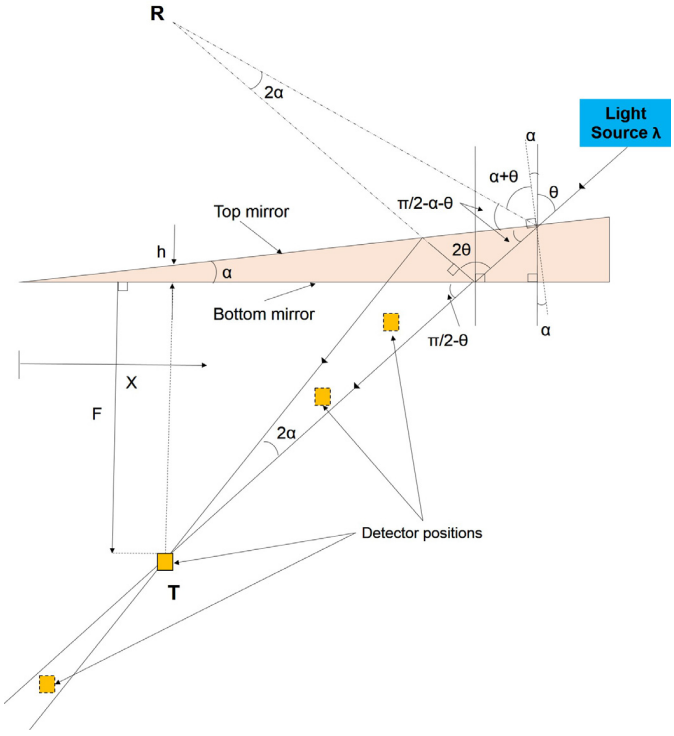

Fig. 8. Geometrically obtained focal points for transmitted (T) and reflected (R) rays as well as possible placement of detector elements. The acute angle at points T and R is 2α. For the best collection of transmitted light, it is preferred to locate the detector at T. In this work, only $\theta < 0$ is considered.

using Fabry-Perot model was measured to be 150 nm. The broadening of FWHM and the decrease in transmitted intensity are consequences of a change in α.

A geometrical analysis of a LVOF is shown in Fig 8. For simplicity, a single light ray of wavelength λ was incidence-d on the tilted top mirror at angle $\theta < 0$ [43]. Although multiple roundtrip internal reflections occur in the cavity gap, only the first and second transmission rays are taken into account in this analysis. This approach is possible as the first two rays are more intense than subsequent internally reflected rays due to transmission loss at every mirror interface. It is shown that the focus at points T and R depends only on the wedge angle, 2α.

Importantly, wedge angle would dictate the detector site location. Thus, it is crucial to position the detector properly for maximum capture of transmitted or reflected light. Placement of detector with respect to the LVOF bottom mirror could be approximated using the following design rule (4) according to Meyer [44]:

$$F \sim \frac{h\theta}{\alpha} \tag{4}$$

where F is the focal point of all converged transmitted rays, h is the thickness of the cavity gap measured perpendicularly to the surface of the bottom mirror. Taking this work as an example, when θ is 0.1°, α is 0.022° and h to be 2.5 and 1 μm for the maximum and minimum cavity gap distance, F then varies between 4.54 and 11.36 μm, respectively along the length of the LVOF. At present, linear array detector elements which are commonly hundreds of micrometer in dimension are large enough to accommodate minute differences.

However, next-generation nano-size photo- or thermal- detectors with much smaller elements such as [45] might have to be tilted at an angle with respect to the LVOF. The concept of tilt-stacking using PR as proposed in this work could also be used to stack LVOF on detector chips.

Such a LVOF can be utilized to analyze sample quickly within its operating range. In this instance, the fabricated LVOF could be effectively deployed for VOCs detection. The presence of C-H is present in all VOCs. C-H peaks are generally present between 3.30 – 3.60 μm. In the presence of a high resolution optical engine, various kinds of hydrocarbon containing chemicals can be tested and discriminated against one another. In addition, the quantity of the hydrocarbon can be derived by merit of Beer-Lambert's law. The law states that absorption (loss in transmission %) is proportional to the concentration of chemical species present. The authors purport that the spectrometer can be deployed for VOC and toxic gases monitoring.

To demonstrate the filter's capability for VOC detection, LVOF with AZ 5214E stumps was tested. Ethanol up to 0.152 ml was dispensed and heated in a tightly enclosed borosilicate glass petri dish. The gas cell which measures approximately 10 mm in height acts as a single pass cell. Prior to measurement, a leak test was conducted as EtOH leakage from the gas cell could cause erroneous reading. It was measured that 0.0001 ml/s of EtOH was lost to the environment. Since the loss was less than 1 % of the total amount of EtOH dispensed, it could be assumed that atmospheric loss was near negligible.

Upon complete vaporization of EtOH at 75 °C, the petri dish was quickly placed on the FTIR sample chuck. The transmission curves when different amount of EtOH was dispensed could be seen in Fig 9A. In the absence of EtOH, the transmission intensity was approximately 15 %. When the EtOH concentration was increased, the transmission % decreased proportionally as shown in Fig 9B. In this case, transmission (T) = 1- absorption (A) while reflection (R) was assumed to be zero. The amount of syringe dispensed EtOH was determined using a calibrated weighing scale. On average, one drop of dispensed EtOH equals to 0.022 ml of EtOH. It can be observed that as the amount of EtOH present in the gas cell increases, the transmission intensity decreases proportionally. The observed drop in the optical transmission is a direct result of absorption by EtOH molecules. In this case, 3.5 μm excitation was chosen specifically as EtOH molecules strongly absorb at that wavelength. One can notice a red-shift in passband from 3.50 μm to about 3.57 μm when EtOH concentration increases. Similar red-shifting phenomenon was reported previously [46]. Effective optical measurement window was constrained to be shorter than 4.50 μm due to the use of borosilicate glass cell.

In addition to the EtOH absorption test performed, as shown above, FDTD simulation was performed to investigate the effect of temperature on the shifting of transmission wavelength. This was deliberately done because EtOH was heated prior to optical measurement. As a result, during FTIR scanning, the temperature of the gas cell and its content were elevated above room temperature. On the other hand, non-EtOH filled gas cell was not heated prior to the experiment. FDTD simulations were then performed at 80, 50 and 25 °C. As shown in Fig 10, no detectable shift in wavelength, as well as a change in transmission characteristics and intensity, were observed in all three cases. Also, the simulated results affirm that such spectrometric analysis can be conducted in a myriad of conditions with little interference from a change in temperature up to 80 °C.

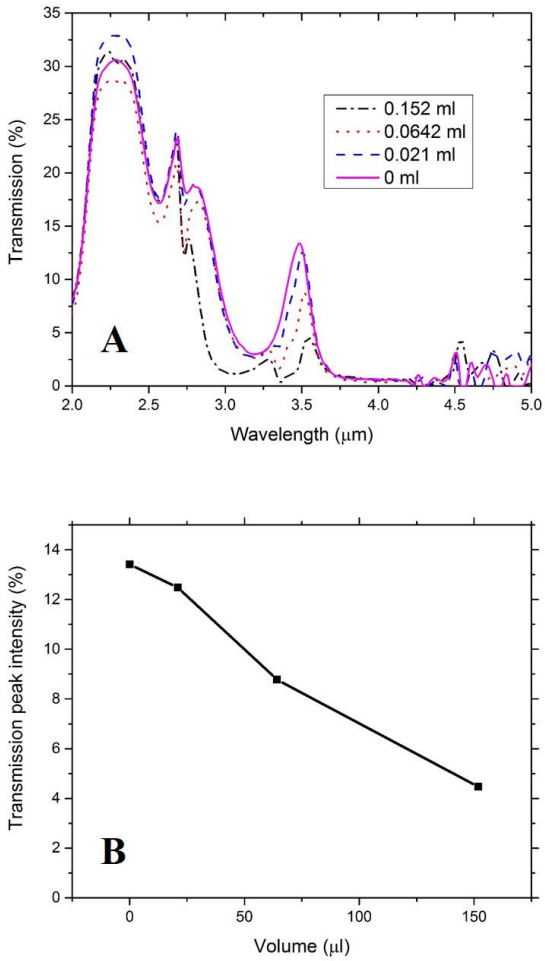

Fig. 9. A) Attenuation of transmission intensity of peak at 3.50 μm when the LVOF was tested with EtOH. The decrease in transmission intensity is proportional to the amount of EtOH vapor presents in the single optical pass gas cell as shown in Fig 9B.

V. Future Outlook

This work was performed to demonstrate the possibility of creating highly precise and optically flat LVOF. Lithographically patterned PR stumps were thermally reflowed to affix two surface micromachined DBR-on –Si wafers to create a predetermined wedge angle. The entire setup was simplified by patterning PR on one edge of the filter while the opposite edge was supported by the bottom substrate. In the future, the two mirrors should be anchored by more pillars and other supporting structures to improve its mechanical integrity. Given the ease of fabrication, the proposed fabrication method can be utilized to design LVOFs with different dimensions and wedge angles for use at various wavelengths.

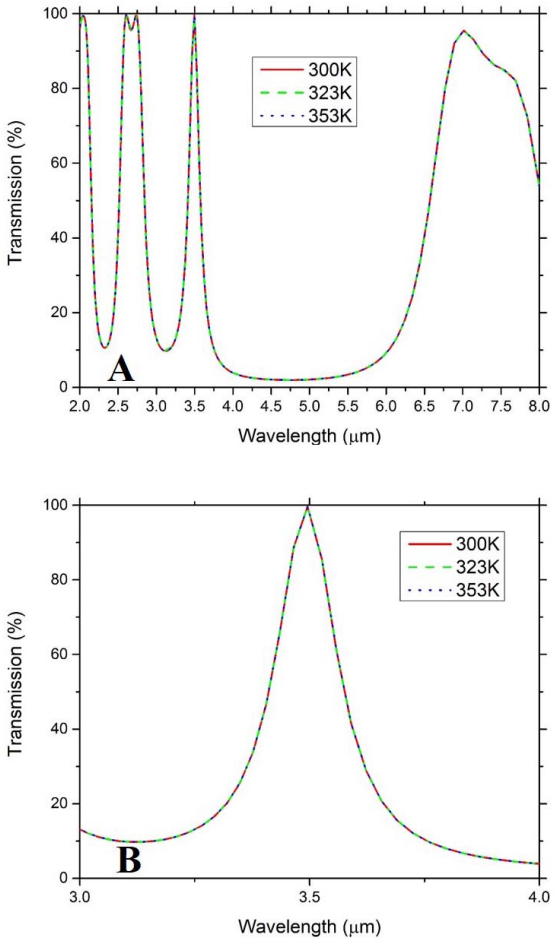

Fig. 10. A) FDTD simulated transmission profiles of the experiment was conducted at various temperatures. It can be observed that molecular absorption is independent of operating temperature. B) Zoomed-in profile of peak at 3.50 μm. Based on simulation results, EtOH absorption test can be conducted up to EtOH boiling point without affecting transmission intensity.

While die-die bonded LVOF was demonstrated in this work, die-wafer level processing can be achieved with the use of an automated die bonder. In this way, PR stumps are patterned onto the entire wafer. Those wafers with poor stump profile can be re-patterned with PR, if needed. This is followed by flipping the diced top die onto the bottom substrate and then subject to thermal reflow. Furthermore, diced filters which have debonded can be reworked by die bonding.

The concept of using PR as stacks can be extended to vertical integration of optical components. For example, an on-chip lens can be placed a fixed distance away from the LVOF by selecting an appropriate PR. Apart from LVOF fabrication, the described fabrication technique can be possibly extended for use in other fields. One such consideration would be to stacking and anchoring chips on top of conductive PR pillars for the formation of low power three-dimensional integrated circuits (3D ICs) [47].

VI. Conclusion

LVOFs fabricated using PR stumps as tilt-stacks between two Si wafers with Si-SiO_2 DBR layers were presented. The step height of the PR could be modulated by spin speed as well as by changing the PR in use. In all, three different PRs, AZ 5214E, AZ 9260 and AZ 4260 were demonstrated as stumps. Fabricated pillar heights of 2.5, 5.4 and 9.6 μm were achieved. These step heights corresponded to wedge angles between the top and bottom wafers to be 0.0205°, 0.0442° and 0.0786°, respectively. The LVOFs made with AZ 5214E, AZ9260 and AZ 4260 had FWHM of 220, 250 and 320 nm at 3.70 μm. It was observed that transmission intensity decreased with an increase in the wedge angle. Transmission intensities at 3.70μm were as follows: 15 % (AZ 5214E), 12 % (AZ 9620) and 10 % (AZ 4260). Thereafter, AZ 5214E fabricated LVOF was subjected to EtOH vapour testing performed at 3.50 μm. The operating range was found to vary inversely proportional to wedge angle such that AZ 5214E LVOF afforded an operating range of 1.75 μm while the operating range of AZ 9260 was 1.25 μm. Transmission intensity decreased from approximately 15 % to 5 % when the volume of EtOH increased from 0 to 0.152 ml.

Acknowledgment

SCKG would like to thank EDB Singapore for supporting the EDB-IPP-Excelitas Industrial Postgraduate Program (IPP). The authors are grateful to KaiLiang Chuan (Excelitas Technologies) for the time spent during project discussion.

References

[1] A. Hursthouse, "Environmental impact of the chemical industry," in *An Introduction to Industrial Chemistry*, A. Heaton, Ed. Dordrecht, The Netherlands: Springer, 1996, pp. 251–288.

[2] L. Fazzo *et al.*, "Hazardous waste and health impact: A systematic review of the scientific literature," *Environ. Health*, vol. 16, no. 1, p. 107, 2017.

[3] S. Giannoukos, B. Brkić, S. Taylor, A. Marshall, and G. F. Verbeck, "Chemical sniffing instrumentation for security applications," *Chem. Rev.*, vol. 116, no. 14, pp. 8146–8172, 2016.

[4] T. Yamate, G. Fujisawa, and T. Ikegami, "Optical sensors for the exploration of oil and gas," *J. Lightw. Technol.*, vol. 35, no. 16, pp. 3538–3545, Aug. 15, 2017.

[5] W. Mihoubi, E. Sahli, A. Gargouri, and C. Amiel, "FTIR spectroscopy of whole cells for the monitoring of yeast apoptosis mediated by p53 over-expression and its suppression by Nigella sativa extracts," *PLoS ONE*, vol. 12, no. 7, 2017, Art. no. e0180680.

[6] P. Edwards *et al.*, "Smartphone based optical spectrometer for diffusive reflectance spectroscopic measurement of hemoglobin," *Sci. Rep.*, vol. 7, Sep. 2017, Art. no. 12224.

[7] A. J. S. McGonigle *et al.*, "Smartphone spectrometers," *Sensors*, vol. 18, p. 223, Jan. 2018.

[8] L. S. Rothman *et al.*, "The HITRAN molecular spectroscopic database and hawks (HITRAN atmospheric workstation): 1996 edition," *J. Quant. Spectrosc. Radiat. Transf.*, vol. 60, no. 5, pp. 665–710, 1998.

[9] T. Tanahashi, M. Toda, H. Miyashita, and T. Ono, "Miniature Fourier transform infrared spectrometer for middle infrared wavelength range," in *Proc. 17th Int. Conf. Solid-State Sens., Actuators Microsyst. (TRANSDUCERS & EUROSENSORS XXVII)*, Jun. 2013, pp. 2509–2512.

[10] S. H. Kong, D. D. L. Wijngaards, and R. F. Wolffenbuttel, "Infrared micro-spectrometer based on a diffraction grating," *Sens. Actuators A, Phys.*, vol. 92, nos. 1–3, pp. 88–95, 2001.

[11] D. W. Warren, J. A. Hackwell, and D. J. Gutierrez, "Compact prism spectrographs based on aplanatic principles," *Opt. Eng.*, vol. 36, no. 4, pp. 1174–1182, 1997.

[12] C. P. Ho, P. Pitchappa, P. Kropelnicki, J. Wang, Y. Gu, and C. Lee, "Development of polycrystalline silicon based photonic crystal membrane for mid-infrared applications," *IEEE J. Sel. Topics Quantum Electron.*, vol. 20, no. 4, pp. 94–100, Jul./Aug. 2014.

[13] A. Rissanen *et al.*, "MEMS Fabry–Perot interferometer based spectral sensors for industrial applications," in *Proc. Imag. Appl. Opt. (3D, AIO, COSI, IS, MATH, pcAOP)*, San Francisco, CA, USA, 2017, Paper ATu1A.1.

[14] M. Erfan, Y. M. Sabry, M. Sakr, B. Mortada, M. Medhat, and D. Khalil, "On-chip micro–electro–mechanical system Fourier transform infrared (MEMS FT-IR) spectrometer-based gas sensing," *Appl. Spectrosc.*, vol. 70, pp. 897–904, May 2016.

[15] H. Huang *et al.*, "Determination of mechanical properties of PECVD silicon nitride thin films for tunable MEMS Fabry–Pérot optical filters," *J. Micromech. Microeng.*, vol. 15, pp. 608–614, Jan. 2005.

[16] L. Comolli and B. Saggin, "Evaluation of the sensitivity to mechanical vibrations of an IR Fourier spectrometer," *Rev. Sci. Instrum.*, vol. 76, no. 12, 2005, Art. no. 123112.

[17] B. Fischer, "Miniaturized all-optical sound pressure sensor," in *Proc. INTER-NOISE NOISE-CON Congr. Conf.*, vol. 253, 2016, pp. 6376–6382.

[18] M. Dami *et al.*, "Ultra compact spectrometer using linear variable filters," in *Proc. Int. Conf. Space Opt.*, vol. 10565, 2018, Art. no. 1056559.

[19] N. P. Ayerden, G. de Graaf, and R. F. Wolffenbuttel, "Compact gas cell integrated with a linear variable optical filter," *Opt. Express*, vol. 24, pp. 2981–3002, Feb. 2016.

[20] A. Emadi *et al.*, "Fabrication and characterization of IC-compatible linear variable optical filters with application in a micro-spectrometer," *Sens. Actuators A, Phys.*, vol. 162, pp. 400–405, Aug. 2010.

[21] P. Ji, C.-S. Park, S. Gao, S.-S. Lee, and D.-Y. Choi, "Angle-tolerant linear variable color filter based on a tapered etalon," *Opt. Express*, vol. 25, pp. 2153–2161, Feb. 2017.

[22] B. Sheng, P. Chen, C. Tao, R. Hong, Y. Huang, and D. Zhang, "Linear variable filters fabricated by ion beam etching with triangle-shaped mask and normal film coating technique," *Chin. Opt. Lett.*, vol. 13, Dec. 2015, Art. no. 122301.

[23] L. Abel-Tiberini, F. Lemarquis, G. Marchand, L. Roussel, G. Albrand, and M. Lequime, "Manufacturing of linear variable filters with straight iso-thickness lines," *Proc. SPIE*, vol. 5963, Oct. 2005, Art. no. 59630B.

[24] L. Liu, H. A. Khan, J. Li, A. C. Hillier, and M. Lu, "A strain-tunable nanoimprint lithography for linear variable photonic crystal filters," *Nanotechnology*, vol. 27, Jun. 2016, Art. no. 295301.

[25] M. Fritze *et al.*, "Fabrication of three-dimensional mode converters for silicon-based integrated optics," *J. Vac. Sci. Technol. B, Microelectron. Nanometer Struct. Process., Meas., Phenomena*, vol. 21, no. 6, pp. 2897–2902, 2003.

[26] S. C. K. Goh, L. L. Shiau, N. Chen, S. Wang, K. Chuan, and H. Ernst, "Low cost rapid fabrication of vertical LVOF microspectrometer on-chip for MIR sensing," *Proc. SPIE*, vol. 10657, May 2018, Art. no. 106570E.

[27] E. Huang, Q. Ma, and Z. Liu, "Etalon array reconstructive spectrometry," *Sci. Rep.*, vol. 7, Nov. 2017, Art. no. 40693.

[28] P. E. Buchsbaum and J. D. Lane, "Tunable variable bandpass optical filter," U.S. Patent 6 700 690, Mar. 2, 2004.

[29] S. C. K. Goh, N. Chen, L. L. Shiau, B. K. Tay, C. Lee, and C. S. Tan, "Deposited poly-Si as on-demand linewidth compensator for on-chip Fabry–Perot interferometer and vertical linear variable optical filter bandpass and passband manipulation," *J. Micromech. Microeng.*, vol. 29, Feb. 2019, Art. no. 047001.

[30] N. P. Ayerden and R. F. Wolffenbuttel, "How accurate is the Fabry–Perot approximation in high-finesse linear variable optical filters for gas absorption spectroscopy?" in *Proc. 19th Int. Conf. Solid-State Sens., Actuators Microsyst. (TRANSDUCERS)*, Jun. 2017, pp. 2111–2114.

[31] T. T. Kajava, H. M. Lauranto, and R. R. E. Salomaa, "Fizeau interferometer in spectral measurements," *J. Opt. Soc. Amer. B, Opt. Phys.*, vol. 10, pp. 1980–1989, Nov. 1993.

[32] E. Johlin *et al.*, "Structural origins of intrinsic stress in amorphous silicon thin films," *Phys. Rev. B, Condens. Matter*, vol. 85, Feb. 2012, Art. no. 075202.

[33] Y. Han *et al.*, "An amorphous Si material with a sponge-like structure as an anode for Li-ion and Na-ion batteries," *Nanoscale*, vol. 10, pp. 3153–3158, 2018.

[34] J. Lee, M. Shon, and J. H. Lyou, "The enhancement of nanocrystallization in amorphous silicon thin films deposited on glass substrate," *Current Appl. Phys.*, vol. 6, pp. e54–e57, Aug. 2006.

[35] H. Shaik, V. Anand, and M. G. Rao, "On the quality of hydrogenated amorphous silicon deposited by sputtering," *Mater. Sci. Semicond. Process.*, vol. 26, pp. 367–373, Oct. 2014.

[36] S. Schröder, A. Duparré, L. Coriand, A. Tünnermann, D. H. Penalver, and J. E. Harvey, "Modeling of light scattering in different regimes of surface roughness," *Opt. Express*, vol. 19, no. 10, pp. 9820–9835, May 2011.

[37] M. Ghaderi *et al.*, "Design, fabrication and characterization of infrared LVOFs for measuring gas composition," *J. Micromech. Microeng.*, vol. 24, Jul. 2014, Art. no. 084001.

[38] B. Liu, Q. Zhao, and P. Zheng, "Optical properties of amorphous silicon thin films fabricated by RF magnetron sputtering," *Proc. SPIE*, vol. 7279, Feb. 2009, Art. no. 72791W.

[39] J.-C. Tsai and Y.-S. Hsu, "Profile of microlens fabricated by the thermal reflow process," *IEEE Trans. Magn.*, vol. 47, no. 3, pp. 598–601, Mar. 2011.

[40] P. Nussbaum, R. Völkel, H. P. Herzig, M. Eisner, and S. Haselbeck, "Design, fabrication and testing of microlens arrays for sensors and microsystems," *Pure Appl. Opt., J. Eur. Opt. Soc. A*, vol. 6, no. 6, pp. 617–636, 1997.

[41] *Products—ASM Pacific Technology*. Accessed: Jun. 25, 2019. [Online]. Available: http://www1.asmpacific.com/en/products?equipment=1

[42] E. Garmire, "Theory of quarter-wave-stack dielectric mirrors used in a thin Fabry–Perot filter," *Appl. Opt.*, vol. 42, pp. 5442–5449, Sep. 2003.

[43] E. Stoykova and M. Nenchev, "Gaussian beam interaction with an air-gap Fizeau interferential wedge," *J. Opt. Soc. Amer. A, Opt. Image Sci.*, vol. 27, pp. 58–68, Jan. 2010.

[44] Y. H. Meyer, "Fringe shape with an interferential wedge," *J. Opt. Soc. Amer.*, vol. 71, pp. 1255–1263, Oct. 1981.

[45] X. Jia, C. Tang, R. Pan, Y. Long, C. Gu, and J. Li, "Thickness-dependently enhanced photodetection performance of vertically grown SnS_2 nanoflakes with large size and high production," *ACS Appl. Mater. Interfaces*, vol. 10, pp. 18073–18081, May 2018.

[46] Y. Wan *et al.*, "Compact characterization of liquid absorption and emission spectra using linear variable filters integrated with a CMOS imaging camera," *Sci. Rep.*, vol. 6, Jul. 2016, Art. no. 29117.

[47] N. Hauptman, M. Žveglič, M. Maček, and M. K. Gunde, "Carbon based conductive photoresist," *J. Mater. Sci.*, vol. 44, pp. 4625–4632, Sep. 2009.